Commun. Comput. Phys.
doi: 10.4208/cicp.OA-2024-0117

Vol. **38**, No. 1, pp. 156-180
July 2025

Low-Dissipation Central-Upwind Schemes for Elasticity in Heterogeneous Media

Alexander Kurganov[1,2,3], Zepei Liu[1], Michael Pollack[4] and Ruixiao Xin[1,*]

[1] *Department of Mathematics, Southern University of Science and Technology, Shenzhen 518055, P.R. China.*
[2] *Shenzhen International Center for Mathematics, Southern University of Science and Technology, Shenzhen 518055, P.R. China.*
[3] *Guangdong Provincial Key Laboratory of Computational Science and Material Design, Southern University of Science and Technology, Shenzhen 518055, P.R. China.*
[4] *Department of Mathematics, Columbia State Community College, Columbia, TN 38401, USA.*

Received 17 May 2024; Accepted (in revised version) 22 October 2024

Abstract. We develop new low-dissipation central-upwind (LDCU) schemes for nonlinear elasticity equations in heterogeneous media. In general, central-upwind schemes belong to the class of finite-volume Godunov-type schemes, which consist of three steps: reconstruction, evolution, and projection onto the original grid. In our new method, the evolution is performed in the standard way by integrating the system over the space-time control volumes. However, the reconstruction and projection are performed in a special manner. First, we take into account the fact that the conservative variables (strain and momentum) are discontinuous across the material interfaces, while the flux variables (velocity and strain) are continuous there: we therefore reconstruct the flux variables. Second, we use a special projection recently introduced in [A. Kurganov and R. Xin, J. Sci. Comput., 96, 2023] to complete the derivation of the LDCU scheme. Our numerical experiments demonstrate that the developed schemes are capable of accurately resolving waves with dispersive behavior that over a long period of time evolve into solitary waves.

AMS subject classifications: 65M08, 76M12, 35L65, 74B20

Key words: Hyperbolic systems of conservation laws, low-dissipation central-upwind schemes, nonlinear elasticity, heterogeneous media, waves with dispersive behavior, solitary waves.

*Corresponding author. *Email addresses:* alexander@sustech.edu.cn (A. Kurganov), 12232862@mail.sustech.edu.cn (Z. Liu), mpollack@ColumbiaState.edu (M. Pollack), 12331009@mail.sustech.edu.cn (R. Xin)

1 Introduction

Consider the one-dimensional (1-D) elasticity system

$$\begin{aligned}&\varepsilon_t-u_x=0,\\&\big(\rho(x)u\big)_t-\sigma_x\big(K(x);\varepsilon\big)=0,\end{aligned}\tag{1.1}$$

where $\varepsilon(x,t)$ is the strain, $u(x,t)$ is the velocity, $\rho(x)$ is the density, $K(x)$ is the bulk modulus of compressibility, and $\sigma(K(x);\varepsilon)$ is the stress. If $\rho(x)$ and $K(x)$ are both constants, then the medium is homogeneous. A nonconstant $\rho(x)$ and $K(x)$ correspond to a heterogeneous medium. We consider a layered medium consisting of two different materials of length ℓ with densities ρ_1 and ρ_2 and bulk moduli of compressibility K_1 and K_2 so that for all integer j,

$$\begin{aligned}\rho(x)&=\begin{cases}\rho_1, & \text{if}\quad 2j\ell<x<(2j+1)\ell,\\ \rho_2, & \text{otherwise},\end{cases}\\ K(x)&=\begin{cases}K_1, & \text{if}\quad 2j\ell<x<(2j+1)\ell,\\ K_2, & \text{otherwise}.\end{cases}\end{aligned}\tag{1.2}$$

The stress-strain relation in the linear case has the form $\sigma_i(\varepsilon)=K_i\varepsilon, i=1,2$. A more realistic model is obtained when a nonlinear stress-strain relation is considered. We take either

$$\sigma_i(\varepsilon)=K_i\varepsilon+\beta K_i^2\varepsilon^2,\quad i\in\{1,2\},\quad \beta=\text{Const}\tag{1.3}$$

or

$$\sigma_i(\varepsilon)=e^{K_i\varepsilon}-1,\quad i\in\{1,2\}\tag{1.4}$$

as examples of such relations; see [6,12,18–20]. In a homogeneous medium with a nonlinear stress-strain relation, a generic solution of (1.1) and (1.3) will typically develop shock and rarefaction waves. But in a heterogeneous medium with a nonlinear stress-strain relation, the resulting waves will have dispersive behaviors that will lead to solitary waves instead of shock waves [6, 12, 17–20].

The elasticity system (1.1) can be put into the framework of conservation laws with space-dependent flux. To this end, we rewrite (1.1) as

$$\boldsymbol{U}_t+\boldsymbol{F}(\mathbf{C}(x);\boldsymbol{U})_x=\mathbf{0},\tag{1.5}$$

where

$$\boldsymbol{U}=(\varepsilon,m)^\top,\quad \boldsymbol{F}\big(\mathbf{C}(x);\boldsymbol{U}\big)=\left(-\frac{m}{\rho(x)},-\sigma\big(K(x);\varepsilon\big)\right)^\top,\tag{1.6}$$

$m=\rho u$ denotes the momentum, and $\mathbf{C}(x):=(\rho(x),K(x))^\top$.

Since (1.5) is a hyperbolic system of conservation laws, it is very natural to numerically solve it by a finite-volume Godunov-type scheme. Such schemes form a class of

projection-evolution methods in which the solution is first approximated by a global piecewise polynomial function and then evolved in time according to an integral form of (1.5), written over certain space-time control volumes (CVs). The evaluation can be done in an upwind manner by (approximately) solving (generalized) Riemann problems arising at the spatial boundaries between the CVs; see, e.g. [1, 7, 10, 17, 26]). This may, however, be quite complicated or even impossible, depending on the system at hand. Alternatively, the CVs can be selected in such a way that all of the possibly non-smooth nonlinear waves stay inside the CVs so that no Riemann problems have to be (approximately) solved. This leads to non-oscillatory central schemes [11, 21, 23], which may be an attractive alternative to upwind schemes. Though central schemes are robust and efficient, they contain relatively large numerical dissipation, which may significantly oversmear contact waves and material interfaces. A way to reduce the numerical dissipation present in central schemes was proposed in [15], where the first central-upwind (CU) scheme was developed. In general, CU schemes take advantage of the simplicity of Riemann-problem-solver-free central schemes while incorporating several upwind features, which help to reduce numerical dissipation; see [3, 13, 14, 16].

Although the aforementioned finite-volume schemes were designed for the systems of conservation laws like $\boldsymbol{U}_t+\boldsymbol{F}(\boldsymbol{U})_x=\boldsymbol{0}$, some of them can be extended to the studied systems with space-dependent fluxes (1.5). This was done in [6], where the wave propagation methods were developed for acoustics problems in periodic or random media, which were extended to the studied system (1.5)-(1.6) in [18] and then applied to nonlinear layered media in [19, 20]. Discontinuous Galerkin methods for the studied system were applied in [2, 24]. In [28], a δ-mapping algorithm originally introduced in [29, 30] for general hyperbolic conservation law with space-dependent fluxes, was coupled with a WENO reconstruction and extended to (1.5)-(1.6).

The goal of this paper is to develop CU schemes for (1.5)-(1.6). In principle, Riemann-problem-solver-free CU schemes can be directly applied to the studied system. However, this may lead to a poor resolution in the case of layered material as we demonstrate in Section 4. In order to prevent this, we develop a low-dissipation CU scheme for (1.5)-(1.6). The LDCU schemes have been recently introduced in [16] and applied to several hyperbolic system of conservation laws in [4, 5, 16]. The key idea of the LDCU schemes is to accurately project the evolved (in time) solution onto the original finite-volume mesh. The projection is based on a subcell reconstruction, which allows one to achieve a very sharp resolution of contact waves/material interfaces.

The rest of the paper is organized as follows. The LDCU scheme for the 1-D elasticity system (1.5)-(1.6) is described in Section 2. It is extended to the 2-D case in Section 3. Finally, in Section 4, we present numerical examples, which clearly demonstrate that the developed schemes are capable of accurately resolving waves with dispersive behavior over a small time scale. The schemes perform extremely well over a long period of time when the waves with dispersive behavior evolve into solitary waves. Moreover, we demonstrate that the LDCU scheme is capable to outperform some of the existing upwind schemes.

2 One-dimensional LDCU scheme

In this section, we develop a second-order LDCU scheme for (1.5)-(1.6). We follow a general framework introduced in [16].

2.1 Fully discrete LDCU scheme

We first introduce a uniform mesh consisting of the finite-volume cells $C_j:=[x_{j-\frac{1}{2}},x_{j+\frac{1}{2}}]$ of size $x_{j+\frac{1}{2}}-x_{j-\frac{1}{2}}\equiv\Delta x$ centered at $x_j=(x_{j-\frac{1}{2}}+x_{j+\frac{1}{2}})/2$, and assume that the solution, realized in terms of its cell averages

$$\overline{\boldsymbol{U}}_j^n\approx\frac{1}{\Delta x}\int_{C_j}\boldsymbol{U}(x,t^n)\mathrm{d}x$$

is available at a certain time level $t=t^n$. A fully discrete LDCU scheme is developed in the following three consecutive steps: reconstruction, evolution, and projection.

Step 1: Reconstruction. Given the cell averages $\{\overline{\boldsymbol{U}}_j^n\}$, our goal is to reconstruct a global (in space) second-order interpolant of $\boldsymbol{U}$ at time $t=t^n$. This can be done with the help of the following piecewise linear reconstruction:

$$\widetilde{\boldsymbol{U}}(x,t^n)=\sum_j\left[\overline{\boldsymbol{U}}_j^n+(\boldsymbol{U}_x)_j^n(x-x_j)\right]\mathcal{X}_{C_j}(x),\tag{2.1}$$

where $\mathcal{X}_{C_j}(x)$ is the characteristic function over the cell C_j and $(\boldsymbol{U}_x)_j^n$ are the slopes, which should approximate the values of $\boldsymbol{U}_x(x_j,t^n)$ with at least first order of accuracy. To make the reconstruction (2.1) non-oscillatory, the slopes are to be computed using a nonlinear limiter; see, e.g. [7,10,17,22,23,25,27]. For instance, one can use the generalized minmod limiter [22,23,25],

$$(\boldsymbol{U}_x)_j^n=\mathrm{minmod}\left(\theta\frac{\overline{\boldsymbol{U}}_{j+1}^n-\overline{\boldsymbol{U}}_j^n}{\Delta x},\frac{\overline{\boldsymbol{U}}_{j+1}^n-\overline{\boldsymbol{U}}_{j-1}^n}{2\Delta x},\theta\frac{\overline{\boldsymbol{U}}_j^n-\overline{\boldsymbol{U}}_{j-1}^n}{\Delta x}\right),\tag{2.2}$$

which can be applied in a componentwise manner. Here,

$$\mathrm{minmod}(z_1,z_2,\ldots,z_m):=\begin{cases}\min(z_1,z_2,\ldots,z_m), & \text{if}\quad z_i>0,\quad\forall i=1,\ldots,m,\\ \max(z_1,z_2,\ldots,z_m), & \text{if}\quad z_i<0,\quad\forall i=1,\ldots,m,\\ 0, & \text{otherwise,}\end{cases}\tag{2.3}$$

and the parameter $\theta\in[1,2]$ can be used to control numerical dissipation. When $\theta=1$, the minmod reconstruction (and thus the resulting scheme) is most dissipative and when $\theta=2$, the minmod reconstruction is least dissipative. In what follows, we will refer to the minmod reconstruction with $\theta=2$ as the MinMod2 reconstruction.

Step 2: Evolution. Next, we need to evolve the approximate solution, represented by a global piecewise linear interpolant $\widetilde{\boldsymbol{U}}(x,t^n)$, to the next time level $t=t^{n+1}:=t^n+\Delta t^n$. To this end, we first estimate the local speeds of propagation

$$a^+_{j+\frac12}=\max\left\{\lambda_+\left(\frac{\partial \boldsymbol{F}}{\partial \boldsymbol{U}}(\mathbf{C}^-_{j+\frac12};\boldsymbol{U}^-_{j+\frac12})\right),\lambda_+\left(\frac{\partial \boldsymbol{F}}{\partial \boldsymbol{U}}(\mathbf{C}^+_{j+\frac12};\boldsymbol{U}^+_{j+\frac12})\right),0\right\},$$

$$a^-_{j+\frac12}=\min\left\{\lambda_-\left(\frac{\partial \boldsymbol{F}}{\partial \boldsymbol{U}}(\mathbf{C}^-_{j+\frac12};\boldsymbol{U}^-_{j+\frac12})\right),\lambda_-\left(\frac{\partial \boldsymbol{F}}{\partial \boldsymbol{U}}(\mathbf{C}^+_{j+\frac12};\boldsymbol{U}^+_{j+\frac12})\right),0\right\},$$

where $\lambda_+>\lambda_-$ are the eigenvalues of the Jacobian $\partial \boldsymbol{F}/\partial \boldsymbol{U}$, and compute the left- and right-sided point values of $\mathbf{C}$ and of the interpolant $\widetilde{\boldsymbol{U}}(x,t^n)$ at $x=x_{j+\frac12}$

$$\mathbf{C}^\pm_{j+\frac12}=\mathbf{C}\big(x_{j+\frac12}\pm0\big),\quad \boldsymbol{U}^+_{j+\frac12}=\overline{\boldsymbol{U}}^n_j-\frac{\Delta x}{2}(\boldsymbol{U}_x)^n_{j+1},\quad \boldsymbol{U}^-_{j+\frac12}=\overline{\boldsymbol{U}}^n_j+\frac{\Delta x}{2}(\boldsymbol{U}_x)^n_j.$$

Note that if $\mathbf{C}$ is continuous at $x_{j+\frac12}$, then $\mathbf{C}^+_{j+\frac12}=\mathbf{C}^-_{j-\frac12}$, but the case of a discontinuous $\mathbf{C}$ is generic. In order to deal with this, we build the grid such that the discontinuities of $\mathbf{C}$ appear at the cell interfaces only.

For the system (1.5)-(1.6), the Jacobian is

$$\frac{\partial \boldsymbol{F}}{\partial \boldsymbol{U}}=\begin{pmatrix}0 & -\dfrac{1}{\rho(x)}\\ -\dfrac{d\sigma}{d\varepsilon} & 0\end{pmatrix},$$

and its eigenvalues are

$$\lambda_\pm(x;\varepsilon)=\pm\sqrt{\frac{d\sigma/d\varepsilon}{\rho(x)}},$$

where for σ given by (1.3) or (1.4),

$$\frac{d\sigma}{d\varepsilon}=K(x)+2\beta K^2(x)\varepsilon\quad\text{or}\quad \frac{d\sigma}{d\varepsilon}=K(x)e^{K(x)\varepsilon},$$

respectively. Since the Riemann fan for the studied system is symmetric, we have $a^+_{j+\frac12}=-a^-_{j+\frac12}=:a_{j+\frac12}$.

We next introduce the points

$$x^n_{j+\frac12,\ell}:=x_{j+\frac12}-a_{j+\frac12}\Delta t^n,\quad x^n_{j+\frac12,r}:=x_{j+\frac12}+a_{j+\frac12}\Delta t^n,$$

and integrate the system (1.5) over the "smooth", $[x_{j-\frac12,r},x_{j+\frac12,\ell}]\times[t^n,t^{n+1}]$, and "non-smooth", $[x_{j+\frac12,\ell},x_{j+\frac12,r}]\times[t^n,t^{n+1}]$, space-time CVs. This way the solution is evolved in

time and upon the completion of the evolution step, we obtain the (intermediate) cell averages

$$\begin{aligned}\overline{\boldsymbol{U}}^{\text{int}}_{j+\frac{1}{2}}&=\frac{\overline{\boldsymbol{U}}^n_j+\overline{\boldsymbol{U}}^n_{j+1}}{2}+\frac{\Delta x-a_{j+\frac{1}{2}}\Delta t^n}{4}\big((\boldsymbol{U}_x)^n_j-(\boldsymbol{U}_x)^n_{j+1}\big)\\&\quad-\frac{1}{2a_{j+\frac{1}{2}}}\Big[\boldsymbol{F}\Big(\mathbf{C}\big(x^n_{j+\frac{1}{2},r}\big);\boldsymbol{U}^{n+\frac{1}{2}}_{j+\frac{1}{2},r}\Big)-\boldsymbol{F}\Big(\mathbf{C}\big(x^n_{j+\frac{1}{2},\ell}\big);\boldsymbol{U}^{n+\frac{1}{2}}_{j+\frac{1}{2},\ell}\Big)\Big],\\\overline{\boldsymbol{U}}^{\text{int}}_{j}&=\overline{\boldsymbol{U}}^n_j+\frac{(\boldsymbol{U}_x)^n_j}{2}\big(a_{j-\frac{1}{2}}-a_{j+\frac{1}{2}}\big)\Delta t^n\\&\quad-\frac{\Delta x}{\Delta x-\big(a_{j-\frac{1}{2}}+a_{j+\frac{1}{2}}\big)\Delta t^n}\Big[\boldsymbol{F}\Big(\mathbf{C}\big(x^n_{j+\frac{1}{2},\ell}\big);\boldsymbol{U}^{n+\frac{1}{2}}_{j+\frac{1}{2},\ell}\Big)-\boldsymbol{F}\Big(\mathbf{C}\big(x^n_{j-\frac{1}{2},r}\big);\boldsymbol{U}^{n+\frac{1}{2}}_{j-\frac{1}{2},r}\Big)\Big],\end{aligned}\tag{2.4}$$

see [13, 16] for details. In (2.4), the point values of $\boldsymbol{U}$ at $(x^n_{j+\frac{1}{2},\ell},t^n)$ and $(x^n_{j+\frac{1}{2},r},t^n)$ are computed using the piecewise linear reconstruction of $\boldsymbol{U}$, namely,

$$\begin{aligned}\boldsymbol{U}^n_{j+\frac{1}{2},\ell}&:=\widetilde{\boldsymbol{U}}\big(x^n_{j+\frac{1}{2},\ell}\big)=\overline{\boldsymbol{U}}^n_j+(\boldsymbol{U}_x)^n_j\left(\frac{\Delta x}{2}-a_{j+\frac{1}{2}}\Delta t^n\right),\\\boldsymbol{U}^n_{j+\frac{1}{2},r}&:=\widetilde{\boldsymbol{U}}\big(x^n_{j+\frac{1}{2},r}\big)=\overline{\boldsymbol{U}}^n_{j+1}-(\boldsymbol{U}_x)^n_{j+1}\left(\frac{\Delta x}{2}-a_{j+\frac{1}{2}}\Delta t^n\right),\end{aligned}$$

and the point values of $\boldsymbol{U}$ at $(x^n_{j+\frac{1}{2},\ell},t^{n+\frac{1}{2}})$ and $(x^n_{j+\frac{1}{2},r},t^{\frac{n+1}{2}})$, are obtained using the Taylor expansions about $(x_{j+\frac{1}{2},r},t^n)$ and $(x_{j+\frac{1}{2},\ell},t^n)$, respectively

$$\begin{aligned}\boldsymbol{U}^{n+\frac{1}{2}}_{j+\frac{1}{2},\ell}&=\boldsymbol{U}^n_{j+\frac{1}{2},\ell}-\frac{\Delta t^n}{2}\boldsymbol{F}\Big(\mathbf{C}\big(x^n_{j+\frac{1}{2},\ell}\big);\boldsymbol{U}^n_{j+\frac{1}{2},\ell}\Big)_x,\\\boldsymbol{U}^{n+\frac{1}{2}}_{j+\frac{1}{2},r}&=\boldsymbol{U}^n_{j+\frac{1}{2},r}-\frac{\Delta t^n}{2}\boldsymbol{F}\Big(\mathbf{C}\big(x^n_{j+\frac{1}{2},r}\big);\boldsymbol{U}^n_{j+\frac{1}{2},r}\Big)_x.\end{aligned}$$

Step 3: Projection. Next, we project the evolved solution realized in terms of its intermediate cell averages $\{\overline{\boldsymbol{U}}^{\text{int}}_j,\overline{\boldsymbol{U}}^{\text{int}}_{j+\frac{1}{2}}\}$, onto the original grid. To this end, we need to construct the interpolant

$$\widetilde{\boldsymbol{U}}^{\text{int}}(x)=\sum_j\Big\{\widetilde{\boldsymbol{U}}^{\text{int}}_{j+\frac{1}{2}}(x)\mathcal{X}_{[x_{j+\frac{1}{2},\ell},x_{j+\frac{1}{2},r}]}+\overline{\boldsymbol{U}}^{\text{int}}_j\mathcal{X}_{[x_{j-\frac{1}{2},r},x_{j+\frac{1}{2},\ell}]}\Big\}.$$

Following [16], we set

$$\widetilde{\boldsymbol{U}}^{\text{int}}_{j+\frac{1}{2}}(x)=\begin{cases}\overline{\boldsymbol{U}}^{\text{int,L}}_{j+\frac{1}{2}}, & x<x_{j+\frac{1}{2}},\\\overline{\boldsymbol{U}}^{\text{int,R}}_{j+\frac{1}{2}}, & x>x_{j+\frac{1}{2}},\end{cases}\tag{2.5}$$

where the values $\overline{\boldsymbol{u}}^{\text{int,L}}_{j+\frac{1}{2}}$ and $\overline{\boldsymbol{u}}^{\text{int,R}}_{j+\frac{1}{2}}$ are determined using the following two requirements. First, from the conservation of ε and m, we have

$$\frac{1}{2}\left(\overline{\boldsymbol{u}}^{\text{int,L}}_{j+\frac{1}{2}}+\overline{\boldsymbol{u}}^{\text{int,R}}_{j+\frac{1}{2}}\right)=\overline{\boldsymbol{u}}^{\text{int}}_{j+\frac{1}{2}}. \tag{2.6}$$

Second, we would like to make sure that σ and u are continuous across the layer interface. Therefore, we take

$$\sigma^{\text{int,L}}_{j+\frac{1}{2}}=\sigma^{\text{int,R}}_{j+\frac{1}{2}},\quad u^{\text{int,L}}_{j+\frac{1}{2}}=u^{\text{int,R}}_{j+\frac{1}{2}},$$

which can be rewritten in terms of the new conservative quantities $\overline{\boldsymbol{u}}^{\text{int,L}}_{j+\frac{1}{2}}$ and $\overline{\boldsymbol{u}}^{\text{int,R}}_{j+\frac{1}{2}}$ as follows:

$$K^-_{j+\frac{1}{2}}\overline{\varepsilon}^{\text{int,L}}_{j+\frac{1}{2}}=K^+_{j+\frac{1}{2}}\overline{\varepsilon}^{\text{int,R}}_{j+\frac{1}{2}},\quad \frac{\overline{m}^{\text{int,L}}_{j+\frac{1}{2}}}{\rho^-_{j+\frac{1}{2}}}=\frac{\overline{m}^{\text{int,R}}_{j+\frac{1}{2}}}{\rho^+_{j+\frac{1}{2}}}. \tag{2.7}$$

After solving the linear system (2.6)-(2.7), we obtain

$$\overline{\boldsymbol{u}}^{\text{int,L}}_{j+\frac{1}{2}}=\begin{pmatrix}\overline{\varepsilon}^{\text{int,L}}_{j+\frac{1}{2}}\\ \overline{m}^{\text{int,L}}_{j+\frac{1}{2}}\end{pmatrix}=\begin{pmatrix}\dfrac{2K^+_{j+\frac{1}{2}}}{K^-_{j+\frac{1}{2}}+K^+_{j+\frac{1}{2}}}\overline{\varepsilon}^{\text{int}}_{j+\frac{1}{2}}\\ \dfrac{2\rho^-_{j+\frac{1}{2}}}{\rho^-_{j+\frac{1}{2}}+\rho^+_{j+\frac{1}{2}}}\overline{m}^{\text{int}}_{j+\frac{1}{2}}\end{pmatrix},$$

$$\overline{\boldsymbol{u}}^{\text{int,R}}_{j+\frac{1}{2}}=\begin{pmatrix}\overline{\varepsilon}^{\text{int,R}}_{j+\frac{1}{2}}\\ \overline{m}^{\text{int,R}}_{j+\frac{1}{2}}\end{pmatrix}=\begin{pmatrix}\dfrac{2K^-_{j+\frac{1}{2}}}{K^-_{j+\frac{1}{2}}+K^+_{j+\frac{1}{2}}}\overline{\varepsilon}^{\text{int}}_{j+\frac{1}{2}}\\ \dfrac{2\rho^+_{j+\frac{1}{2}}}{\rho^-_{j+\frac{1}{2}}+\rho^+_{j+\frac{1}{2}}}\overline{m}^{\text{int}}_{j+\frac{1}{2}}\end{pmatrix}.$$

We now define the auxiliary diagonal matrices $\mathcal{A}^+_{j+\frac{1}{2}}$ and $\mathcal{A}^-_{j+\frac{1}{2}}$

$$\begin{aligned}\mathcal{A}^+_{j+\frac{1}{2}}&:=\begin{pmatrix}\dfrac{2K^-_{j+\frac{1}{2}}}{K^-_{j+\frac{1}{2}}+K^+_{j+\frac{1}{2}}} & 0\\ 0 & \dfrac{2\rho^+_{j+\frac{1}{2}}}{\rho^-_{j+\frac{1}{2}}+\rho^+_{j+\frac{1}{2}}}\end{pmatrix},\\ \mathcal{A}^-_{j+\frac{1}{2}}&:=\begin{pmatrix}\dfrac{2K^+_{j+\frac{1}{2}}}{K^-_{j+\frac{1}{2}}+K^+_{j+\frac{1}{2}}} & 0\\ 0 & \dfrac{2\rho^-_{j+\frac{1}{2}}}{\rho^-_{j+\frac{1}{2}}+\rho^+_{j+\frac{1}{2}}}\end{pmatrix},\end{aligned} \tag{2.8}$$

so that

$$\overline{\boldsymbol{U}}^{\text{int,L}}_{j+\frac{1}{2}}=\mathcal{A}^{-}_{j+\frac{1}{2}}\overline{\boldsymbol{U}}^{\text{int}}_{j+\frac{1}{2}},\quad \overline{\boldsymbol{U}}^{\text{int,R}}_{j+\frac{1}{2}}=\mathcal{A}^{+}_{j+\frac{1}{2}}\overline{\boldsymbol{U}}^{\text{int}}_{j+\frac{1}{2}}. \tag{2.9}$$

After modifying the reconstruction $\widetilde{\boldsymbol{U}}^{\text{int}}$, we perform the projection step to end up with

$$\begin{aligned}\overline{\boldsymbol{U}}^{n+1}_{j}&=\frac{1}{\Delta x}\int\limits_{x_{j-\frac{1}{2}}}^{x_{j+\frac{1}{2}}}\widetilde{\boldsymbol{U}}^{\text{int}}(\xi)\,d\xi=\overline{\boldsymbol{U}}^{\text{int}}_{j}+\frac{\Delta t^n}{\Delta x}\Big[a_{j-\frac{1}{2}}\big(\overline{\boldsymbol{U}}^{\text{int,R}}_{j-\frac{1}{2}}-\overline{\boldsymbol{U}}^{\text{int}}_{j}\big)+a_{j+\frac{1}{2}}\big(\overline{\boldsymbol{U}}^{\text{int,L}}_{j+\frac{1}{2}}-\overline{\boldsymbol{U}}^{\text{int}}_{j}\big)\Big]\\&\overset{(2.9)}{=}\overline{\boldsymbol{U}}^{\text{int}}_{j}+\frac{\Delta t^n}{\Delta x}\Big[a_{j-\frac{1}{2}}\big(\mathcal{A}^{+}_{j-\frac{1}{2}}\overline{\boldsymbol{U}}^{\text{int}}_{j-\frac{1}{2}}-\overline{\boldsymbol{U}}^{\text{int}}_{j}\big)+a_{j+\frac{1}{2}}\big(\mathcal{A}^{-}_{j+\frac{1}{2}}\overline{\boldsymbol{U}}^{\text{int}}_{j+\frac{1}{2}}-\overline{\boldsymbol{U}}^{\text{int}}_{j}\big)\Big].\end{aligned} \tag{2.10}$$

2.2 Semi-discrete LDCU scheme

We now pass to the semi-discrete limit by sending $\Delta t^n\to 0$ in (2.10). This results in

$$\begin{aligned}\frac{\mathrm{d}}{\mathrm{d}t}\overline{\boldsymbol{U}}_j(t^n)&=\lim_{\Delta t^n\to 0}\frac{\overline{\boldsymbol{U}}^{n+1}_{j}-\overline{\boldsymbol{U}}^{n}_{j}}{\Delta t^n}=\lim_{\Delta t^n\to 0}\frac{\overline{\boldsymbol{U}}^{\text{int}}_{j}-\overline{\boldsymbol{U}}^{n}_{j}}{\Delta t^n}\\&+\frac{1}{\Delta x}\Big[a_{j-\frac{1}{2}}\mathcal{A}^{+}_{j-\frac{1}{2}}\lim_{\Delta t^n\to 0}\overline{\boldsymbol{U}}^{\text{int}}_{j-\frac{1}{2}}-\big(a_{j-\frac{1}{2}}+a_{j+\frac{1}{2}}\big)\lim_{\Delta t^n\to 0}\overline{\boldsymbol{U}}^{\text{int}}_{j}+a_{j+\frac{1}{2}}\mathcal{A}^{-}_{j+\frac{1}{2}}\lim_{\Delta t^n\to 0}\overline{\boldsymbol{U}}^{\text{int}}_{j+\frac{1}{2}}\Big].\end{aligned}$$

We then proceed as in [16, Section 2.2] and use the fact that, according to (2.8), $\mathcal{A}^{+}_{j+\frac{1}{2}}+\mathcal{A}^{-}_{j+\frac{1}{2}}\equiv 2I$, to end up with the new semi-discrete LDCU scheme, which can be written in the following flux form:

$$\frac{\mathrm{d}}{\mathrm{d}t}\overline{\boldsymbol{U}}_j=-\frac{\boldsymbol{\mathcal{F}}_{j+\frac{1}{2}}-\boldsymbol{\mathcal{F}}_{j-\frac{1}{2}}}{\Delta x}, \tag{2.11}$$

where the numerical fluxes are

$$\begin{aligned}\boldsymbol{\mathcal{F}}_{j+\frac{1}{2}}&=\frac{\mathcal{A}^{-}_{j+\frac{1}{2}}\boldsymbol{F}\big(\mathbf{C}^{+}_{j+\frac{1}{2}};\boldsymbol{U}^{+}_{j+\frac{1}{2}}\big)+\mathcal{A}^{+}_{j+\frac{1}{2}}\boldsymbol{F}\big(\mathbf{C}^{-}_{j-\frac{1}{2}};\boldsymbol{U}^{-}_{j+\frac{1}{2}}\big)}{2}\\&-\frac{a_{j+\frac{1}{2}}}{2}\Big(\mathcal{A}^{-}_{j+\frac{1}{2}}\boldsymbol{U}^{+}_{j+\frac{1}{2}}-\mathcal{A}^{+}_{j+\frac{1}{2}}\boldsymbol{U}^{-}_{j+\frac{1}{2}}\Big).\end{aligned} \tag{2.12}$$

Note that the indexed quantities in (2.11), (2.12), and most of the formulae below are time-dependent, but we omit this dependence for the sake of brevity.

Remark 2.1. A direct application of the CU scheme from [13] to (1.5)-(1.6) is obtained by replacing (2.5) with the following limited linear piece:

$$\widetilde{\boldsymbol{U}}^{\text{int}}_{j+\frac{1}{2}}(x)=\overline{\boldsymbol{U}}^{\text{int}}_{j+\frac{1}{2}}+(\boldsymbol{U}_x)^{\text{int}}_{j+\frac{1}{2}}\big(x-x_{j+\frac{1}{2}}\big),$$

where the slope $(\boldsymbol{U}_x)^{\text{int}}_{j+\frac{1}{2}}$ is computed as in [13, Section 2]. The corresponding semi-discrete CU scheme will then have the following numerical fluxes:

$$\begin{aligned}\boldsymbol{\mathcal{F}}_{j+\frac{1}{2}}=&\frac{\boldsymbol{F}\big(\mathbf{C}^+_{j+\frac{1}{2}};\boldsymbol{U}^+_{j+\frac{1}{2}}\big)+\boldsymbol{F}\big(\mathbf{C}^-_{j-\frac{1}{2}};\boldsymbol{U}^-_{j+\frac{1}{2}}\big)}{2}\\&-\frac{a_{j+\frac{1}{2}}}{2}\Big[\big(\boldsymbol{U}^+_{j+\frac{1}{2}}-\boldsymbol{U}^-_{j+\frac{1}{2}}\big)-\mathbf{d}_{j+\frac{1}{2}}\Big],\end{aligned}\tag{2.13}$$

which are different from those in (2.12). In (2.13), $\mathbf{d}_{j+\frac{1}{2}}$ is a "built-in" anti-diffusion term given by

$$\mathbf{d}_{j+\frac{1}{2}}=\text{minmod}\Big(\boldsymbol{U}^+_{j+\frac{1}{2}}-\boldsymbol{U}^*_{j+\frac{1}{2}},\boldsymbol{U}^*_{j+\frac{1}{2}}-\boldsymbol{U}^-_{j+\frac{1}{2}}\Big),$$

$$\boldsymbol{U}^*_{j+\frac{1}{2}}=\frac{\boldsymbol{U}^+_{j+\frac{1}{2}}+\boldsymbol{U}^-_{j+\frac{1}{2}}}{2}-\frac{\boldsymbol{F}\big(\mathbf{C}^+_{j+\frac{1}{2}};\boldsymbol{U}^+_{j+\frac{1}{2}}\big)-\boldsymbol{F}\big(\mathbf{C}^-_{j-\frac{1}{2}};\boldsymbol{U}^-_{j+\frac{1}{2}}\big)}{2a_{j+\frac{1}{2}}}.$$

In the numerical results reported in Section 4, we will compare the behavior of this CU scheme with the proposed LDCU one.

2.3 Special reconstruction

The LDCU numerical flux (2.12) should be computed using the reconstructed point values $\boldsymbol{U}^{\pm}_{j+\frac{1}{2}}$. If these values are computed using the MinMod2 reconstruction (2.1)-(2.3), then the computed solution may contain severe oscillations. This occurs since $\overline{\varepsilon}_j$ and $\overline{m}_j$ typically jump across layer interfaces (these are contact discontinuities) so when the MinMod2 limiter is applied to ε and m at cells bordering a layer interface, it may result in a one-sided numerical derivative. Then, even if the resulting reconstruction of ε and m are non-oscillatory, the corresponding point values of u and σ may be oscillatory.

To illustrate such possibility, let us consider a particular set of cell averages of m: $\{\overline{m}_{j-1}=1.5,\overline{m}_j=0.9,\overline{m}_{j+1}=0.25,\overline{m}_{j+2}=0.25\}$ and the corresponding point values of u: $\{u_{j-1}=0.5,u_j=0.3,u_{j+1}=0.25,u_{j+2}=0.25\}$, as shown in Figs. 1 and 2. A MinMod2 reconstruction for m in the cells C_j and C_{j+1} is shown in Fig. 1 (left). A layer interface is located at $x=x_{j+\frac{1}{2}}$ with $\rho=3$ to the left and $\rho=1$ to the right of the layer interface. One can see that while the reconstruction for m is non-oscillatory, the corresponding values of u, obtained through $u=m/\rho$, contain an oscillation at the layer interface; see Fig. 1 (right).

To prevent such oscillations, we use the fact that both u and σ are continuous across a layer interface and apply the limiter to these continuous quantities rather than to ε and m. In Fig. 2 (left), the point values $u^+_{j-\frac{1}{2}},u^-_{j+\frac{1}{2}},u^+_{j+\frac{1}{2}}$, and $u^-_{j+\frac{3}{2}}$ are reconstructed using the MinMod2 limiter. The resulting reconstruction is non-oscillatory and the obtained values of $m=\rho u$ are non-oscillatory as well; see Fig. 2 (right).

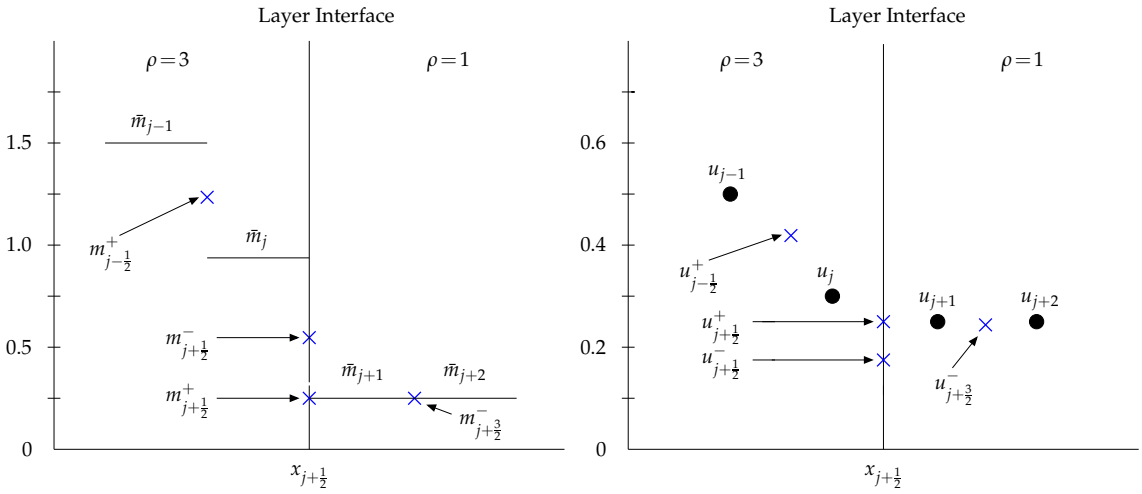

Figure 1: MinMod2 reconstruction applied to the cell averages of m (left) and the obtained point values of $u=m/\rho$ (right). Notice the oscillation in the u-field at $x=x_{j+\frac{1}{2}}$.

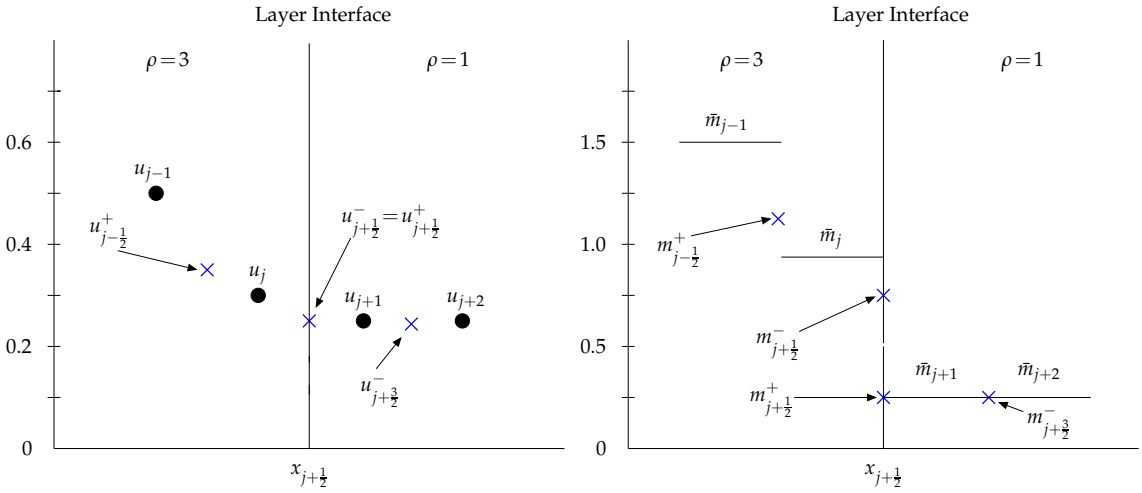

Figure 2: MinMod2 reconstruction applied to the point values of u (left) and the obtained point values of $m=\rho u$ (right). The resulting reconstruction is non-oscillatory.

In the general case, the point values u_j and σ_j are

$$u_j=\frac{\overline{m}_j}{\rho_j},\quad \sigma_j=K_j\overline{\varepsilon}_j+\beta K_j^2(\overline{\varepsilon}_j)^2 \quad \text{or} \quad \sigma_j=e^{K_j\overline{\varepsilon}_j}-1.$$

The reconstructed point values are then

$$u^-_{j+\frac{1}{2}}=u_j+\frac{\Delta x}{2}(u_x)_j,\quad u^+_{j+\frac{1}{2}}=u_{j+1}-\frac{\Delta x}{2}(u_x)_{j+1},$$

$$\sigma^-_{j+\frac{1}{2}}=\sigma_j+\frac{\Delta x}{2}(\sigma_x)_j,\quad \sigma^+_{j+\frac{1}{2}}=\sigma_{j+1}-\frac{\Delta x}{2}(\sigma_x)_{j+1},$$

where the slopes are obtained using, for example, the generalized minmod limiter

$$(u_x)_j=\text{minmod}\left(\theta\frac{u_{j+1}-u_j}{\Delta x},\frac{u_{j+1}-u_{j-1}}{2\Delta x},\theta\frac{u_j-u_{j-1}}{\Delta x}\right),$$

$$(\sigma_x)_j=\text{minmod}\left(\theta\frac{\sigma_{j+1}-\sigma_j}{\Delta x},\frac{\sigma_{j+1}-\sigma_{j-1}}{2\Delta x},\theta\frac{\sigma_j-\sigma_{j-1}}{\Delta x}\right).$$

We can now calculate the corresponding point values of ε and m, which are also used in the calculation of the numerical fluxes. To this end, we introduce the notations

$$\rho^\pm_{j+\frac{1}{2}}:=\rho\big(x_{j+\frac{1}{2}}\pm 0\big),\quad K^\pm_{j+\frac{1}{2}}:=K\big(x_{j+\frac{1}{2}}\pm 0\big),$$

and compute $\varepsilon^\pm_{j+\frac{1}{2}}$ by

$$\varepsilon^\pm_{j+\frac{1}{2}}=\frac{-1+\sqrt{1+4\beta\sigma^\pm_{j+\frac{1}{2}}}}{2\beta K^\pm_{j+\frac{1}{2}}}\quad\text{or}\quad \varepsilon^\pm_{j+\frac{1}{2}}=\frac{\ln\big(\sigma^\pm_{j+\frac{1}{2}}+1\big)}{K^\pm_{j+\frac{1}{2}}},$$

depending on which stress-strain relation, (1.3) or (1.4), is being used.

3 Two-dimensional LDCU scheme

We follow [12] and use a "dimension-by-dimension" approach in order to extend the 1-D system to the following (nonlinear) 2-D elasticity system:

$$\begin{aligned}&\varepsilon_t-u_x-v_y=0,\\&\big(\rho(x,y)u\big)_t-\sigma_x\big(K(x,y);\varepsilon\big)=0,\\&\big(\rho(x,y)v\big)_t-\sigma_y\big(K(x,y);\varepsilon\big)=0,\end{aligned}\tag{3.1}$$

where u and v are the x- and y-velocities, respectively. The system (3.1) can be written as

$$\begin{aligned}&\boldsymbol{U}_t(\mathbf{x},t)+\boldsymbol{F}\big(\mathbf{C}(x);\boldsymbol{U}\big)_x+\boldsymbol{G}\big(\mathbf{C}(y);\boldsymbol{U}\big)_y=\mathbf{0},\\&\boldsymbol{U}=(\varepsilon,m_u,m_v)^\top,\quad \boldsymbol{F}\big(\mathbf{C}(x);\boldsymbol{U}\big)=\left(-\frac{m_u}{\rho},-\sigma,0\right)^\top,\quad \boldsymbol{G}\big(\mathbf{C}(y);\boldsymbol{U}\big)=\left(-\frac{m_v}{\rho},0,-\sigma\right)^\top.\end{aligned}\tag{3.2}$$

Here, $m_u=\rho u$ and $m_v=\rho v$ denote the corresponding momenta and σ is defined as in either (1.3) or (1.4).

The elasticity system (3.2) is relevant when the layers of material are either vertical or horizontal. In this case, one can set up a Cartesian grid for which material interfaces

align with the cell interfaces as, for instance, in Fig. 13 below. In a general 2-D case, the elasticity system is more complicated; see, e.g. [17].

We design the LDCU scheme for the system (3.2) along the same lines as in Section 2. We first introduce a uniform mesh consisting of the finite-volume cells $C_{j,k}:=[x_{j-\frac{1}{2}},x_{j+\frac{1}{2}}]\times[y_{k-\frac{1}{2}},y_{k+\frac{1}{2}}]$ of the uniform size $\Delta x\Delta y$ with $x_{j+\frac{1}{2}}-x_{j-\frac{1}{2}}\equiv\Delta x$ and $y_{k+\frac{1}{2}}-y_{k-\frac{1}{2}}\equiv\Delta y$ centered at (x_j,y_k) with $x_j=(x_{j-\frac{1}{2}}+x_{j+\frac{1}{2}})/2$ and $y_k=(y_{k-\frac{1}{2}}+y_{k+\frac{1}{2}})/2$, and assume that the cell averages at a certain time level t,

$$\overline{\boldsymbol{U}}_{j,k}\approx\frac{1}{\Delta x\Delta y}\iint_{C_{j,k}}\boldsymbol{U}(x,y,t)\,\mathrm{d}x\mathrm{d}y,$$

are available.

At the reconstruction step, we again (as in Section 2.3) reconstruct the continuous flux variables instead of the discontinuous conservative ones. This means that the point values at the cell centers,

$$\begin{aligned}&u_{j,k}=\frac{(\overline{m}_u)_{j,k}}{\rho_{j,k}},\quad v_{j,k}=\frac{(\overline{m}_v)_{j,k}}{\rho_{j,k}},\\&\sigma_{j,k}=K_{j,k}\overline{\varepsilon}_{j,k}+\beta K_{j,k}^2(\overline{\varepsilon}_{j,k})^2\quad\text{or}\quad\sigma_{j,k}=e^{K_{j,k}\overline{\varepsilon}_{j,k}}-1,\end{aligned}$$

are used to obtain the reconstructed one-sided values at the four sides of the cell $C_{j,k}$

$$\begin{aligned}&u^-_{j+\frac{1}{2},k}=u_{j,k}+\frac{\Delta x}{2}(u_x)_{j,k},\quad u^-_{j,k+\frac{1}{2}}=u_{j,k}+\frac{\Delta y}{2}(u_y)_{j,k},\\&u^+_{j-\frac{1}{2},k}=u_{j,k}-\frac{\Delta x}{2}(u_x)_{j,k},\quad u^+_{j,k-\frac{1}{2}}=u_{j,k}-\frac{\Delta y}{2}(u_y)_{j,k}.\end{aligned}\tag{3.3}$$

To ensure a non-oscillatory nature of the resulting scheme, the slopes in (3.3) are to be computed using a nonlinear limiter. In the numerical experiment reported in Section 4, we have used the MinMod2 limiter

$$\begin{aligned}(u_x)_{j,k}&=\mathrm{minmod}\left(2\frac{u_{j+1,k}-u_{j,k}}{\Delta x},\frac{u_{j+1,k}-u_{j-1,k}}{2\Delta x},2\frac{u_{j,k}-u_{j-1,k}}{\Delta x}\right),\\(u_y)_{j,k}&=\mathrm{minmod}\left(2\frac{u_{j,k+1}-u_{j,k}}{\Delta y},\frac{u_{j,k+1}-u_{j,k-1}}{2\Delta y},2\frac{u_{j,k}-u_{j,k-1}}{\Delta y}\right).\end{aligned}$$

The reconstructed values of the other two flux variables, v and σ, are obtained in a similar way.

We can now calculate the corresponding point values of m_u,m_v, and ε

$$(m_u)^-_{j+\frac{1}{2},k}=\rho^-_{j+\frac{1}{2},k}u^-_{j+\frac{1}{2},k},\quad(m_v)^-_{j+\frac{1}{2},k}=\rho^-_{j+\frac{1}{2},k}v^-_{j+\frac{1}{2},k},\tag{3.4}$$

and $\varepsilon^-_{j+\frac{1}{2},k}$ is computed depending on which stress-strain relation is being used, that is,

by either

$$\varepsilon^-_{j+\frac{1}{2},k}=\frac{-1+\sqrt{1+4\beta\sigma^-_{j+\frac{1}{2},k}}}{2\beta K^-_{j+\frac{1}{2},k}} \quad \text{or} \quad \varepsilon^-_{j+\frac{1}{2},k}=\frac{\ln(\sigma^-_{j+\frac{1}{2},k}+1)}{K^-_{j+\frac{1}{2},k}}. \tag{3.5}$$

In (3.4) and (3.5), $\rho^-_{j+\frac{1}{2},k}:=\rho(x_{j+\frac{1}{2}}-0,y_k)$ and $K^-_{j+\frac{1}{2},k}:=K(x_{j+\frac{1}{2}}-0,y_k)$. All other point values of $\boldsymbol{U}$ along the boundary of cell $C_{j,k}$ are calculated likewise.

The solution is evolved in time by solving the following system of ODEs:

$$\frac{\mathrm{d}}{\mathrm{d}t}\overline{\boldsymbol{U}}_{j,k}=-\frac{\boldsymbol{\mathcal{F}}_{j+\frac{1}{2},k}-\boldsymbol{\mathcal{F}}_{j-\frac{1}{2},k}}{\Delta x}-\frac{\boldsymbol{\mathcal{G}}_{j,k+\frac{1}{2}}-\boldsymbol{\mathcal{G}}_{j,k-\frac{1}{2}}}{\Delta y}, \tag{3.6}$$

where $\boldsymbol{\mathcal{F}}_{j+\frac{1}{2},k}$ and $\boldsymbol{\mathcal{G}}_{j,k+\frac{1}{2}}$ are the 2-D LDCU fluxes, obtained in a "dimension-by-dimension" manner

$$\begin{aligned}\boldsymbol{\mathcal{F}}_{j+\frac{1}{2},k}=&\frac{1}{2}\Big(\mathcal{A}^-_{j+\frac{1}{2},k}\boldsymbol{F}\big(\mathbf{C}^+_{j+\frac{1}{2},k};\boldsymbol{U}^+_{j+\frac{1}{2},k}\big)+\mathcal{A}^+_{j+\frac{1}{2},k}\boldsymbol{F}\big(\mathbf{C}^-_{j+\frac{1}{2},k};\boldsymbol{U}^-_{j+\frac{1}{2},k}\big)\Big)\\&-\frac{1}{2}a_{j+\frac{1}{2},k}\Big(\mathcal{A}^-_{j+\frac{1}{2},k}\boldsymbol{U}^+_{j+\frac{1}{2},k}-\mathcal{A}^+_{j+\frac{1}{2},k}\boldsymbol{U}^-_{j+\frac{1}{2},k}\Big),\end{aligned}$$

$$\begin{aligned}\boldsymbol{\mathcal{G}}_{j,k+\frac{1}{2}}=&\frac{1}{2}\Big(\mathcal{A}^-_{j,k+\frac{1}{2}}\boldsymbol{G}\big(\mathbf{C}^+_{j,k+\frac{1}{2}};\boldsymbol{U}^+_{j,k+\frac{1}{2}}\big)+\mathcal{A}^+_{j,k+\frac{1}{2}}\boldsymbol{G}\big(\mathbf{C}^-_{j,k+\frac{1}{2}};\boldsymbol{U}^-_{j,k+\frac{1}{2}}\big)\Big)\\&-\frac{1}{2}a_{j,k+\frac{1}{2}}\Big(\mathcal{A}^-_{j,k+\frac{1}{2}}\boldsymbol{U}^+_{j,k+\frac{1}{2}}-\mathcal{A}^+_{j,k+\frac{1}{2}}\boldsymbol{U}^-_{j,k+\frac{1}{2}}\Big).\end{aligned}$$

Here, the auxiliary diagonal matrices $\mathcal{A}$ are given by

$$\mathcal{A}^+_{j+\frac{1}{2},k}=\mathrm{diag}\left(\frac{2K^-_{j+\frac{1}{2},k}}{K^-_{j+\frac{1}{2},k}+K^+_{j+\frac{1}{2},k}},\frac{2\rho^+_{j+\frac{1}{2},k}}{\rho^-_{j+\frac{1}{2},k}+\rho^+_{j+\frac{1}{2},k}},0\right),$$

$$\mathcal{A}^-_{j+\frac{1}{2},k}=\mathrm{diag}\left(\frac{2K^+_{j+\frac{1}{2},k}}{K^-_{j+\frac{1}{2},k}+K^+_{j+\frac{1}{2},k}},\frac{2\rho^-_{j+\frac{1}{2},k}}{\rho^-_{j+\frac{1}{2},k}+\rho^+_{j+\frac{1}{2},k}},0\right),$$

$$\mathcal{A}^+_{j,k+\frac{1}{2}}=\mathrm{diag}\left(\frac{2K^-_{j,k+\frac{1}{2}}}{K^-_{j,k+\frac{1}{2}}+K^+_{j,k+\frac{1}{2}}},0,\frac{2\rho^+_{j,k+\frac{1}{2}}}{\rho^-_{j,k+\frac{1}{2}}+\rho^+_{j,k+\frac{1}{2}}}\right),$$

$$\mathcal{A}^-_{j,k+\frac{1}{2}}=\mathrm{diag}\left(\frac{2K^+_{j,k+\frac{1}{2}}}{K^-_{j,k+\frac{1}{2}}+K^+_{j,k+\frac{1}{2}}},0,\frac{2\rho^-_{j,k+\frac{1}{2}}}{\rho^-_{j,k+\frac{1}{2}}+\rho^+_{j,k+\frac{1}{2}}}\right),$$

and the local propagation speeds are estimated by

$$a_{j+\frac{1}{2},k}=\max_{\pm}\sqrt{\frac{(\mathrm{d}\sigma/\mathrm{d}\varepsilon)^{\pm}_{j+\frac{1}{2},k}}{\rho^{\pm}_{j+\frac{1}{2},k}}},\quad a_{j,k+\frac{1}{2}}=\max_{\pm}\sqrt{\frac{(\mathrm{d}\sigma/\mathrm{d}\varepsilon)^{\pm}_{j,k+\frac{1}{2}}}{\rho^{\pm}_{j,k+\frac{1}{2}}}}.$$

4 Numerical examples

In this section, we present both 1-D and 2-D numerical examples. Our main goal is to demonstrate that equipped with the special reconstruction, the LDCU schemes produce non-oscillatory results and also achieve higher resolution than both the CU scheme from [13] and the wave propagation method from [18].

In all of the examples, we have integrated the ODE systems (2.11) and (3.6) using the three-stage third-order strong stability preserving (SSP) Runge-Kutta method (see, e.g. [8,9]) and used the CFL number 0.5.

4.1 One-dimensional examples

Example 1 (Accuracy Test). In the first example taken from [28], we consider the following smooth initial data prescribed on the computational domain $[-1,1]$:

$$\begin{aligned}&\varepsilon(x,0)=12x+24, && u(x,0)=-(12x^2+48x+72),\\ &\rho(x)=\frac{6x^2+26x+28}{x^2+4x+6}, && \sigma(x,0)=\left(\frac{x}{2}+\frac{5}{4}\right)\varepsilon^2(x,0),\end{aligned}$$

and the following Dirichlet conditions:

$$\begin{aligned}&u(-1,t)=-\frac{36}{(t+1)^3}, && u(1,t)=-\frac{132}{(t+1)^3},\\ &\sigma(-1,t)=\frac{108}{(t+1)^4}, && \sigma(1,t)=\frac{2268}{(t+1)^4},\end{aligned}$$

which are implemented as follows. We first set

$$u^-_{\frac12}=u(-1,t),\quad u^+_{N+\frac12}=u(1,t),\quad \sigma^-_{\frac12}=\sigma(-1,t),\quad \sigma^+_{N+\frac12}=\sigma(1,t),$$

where N is the total number of the uniform cells, and then use these values to compute the slopes $(u_x)_1,(u_x)_N,(\sigma_x)_1$, and $(\sigma_x)_N$ in the cells C_1 and C_N:

$$\begin{aligned}(u_x)_1&=\text{minmod}\left(\theta\frac{u_2-u_1}{\Delta x},2\frac{u_1-u^-_{\frac12}}{\Delta x}\right),\\ (u_x)_N&=\text{minmod}\left(\theta\frac{u_N-u_{N-1}}{\Delta x},2\frac{u^+_{N+\frac12}-u_N}{\Delta x}\right),\\ (\sigma_x)_1&=\text{minmod}\left(\theta\frac{\sigma_2-\sigma_1}{\Delta x},2\frac{\sigma_1-\sigma^-_{\frac12}}{\Delta x}\right),\\ (\sigma_x)_N&=\text{minmod}\left(\theta\frac{\sigma_N-\sigma_{N-1}}{\Delta x},2\frac{\sigma^+_{N+\frac12}-\sigma_N}{\Delta x}\right).\end{aligned}$$

We note that the exact solution of this initial-boundary value problem is available and given by

$$\varepsilon(x,t)=\frac{12x+24}{(t+1)^2},\quad u(x,t)=-\frac{12x^2+48x+72}{(t+1)^3}.$$

We now compute the numerical solution until the final time $t=1$ using the LDCU scheme with the minmod parameter $\theta=2$ on a sequence of uniform meshes with $\Delta x=1/5,1/10,1/20,1/40,1/80$, and $1/160$. We then measure the L^1-errors and compute the corresponding experimental convergence rates. The obtained results presented in Table 1, confirm that the second order of accuracy is achieved by the LDCU scheme.

Table 1: Example 1: The L^1-errors and experimental convergence rates for the strain ε and momentum m.

Δx	ε		m	
	Error	Rate	Error	Rate
1/5	1.20e-01	-	6.15e-01	-
1/10	3.34e-02	1.84	1.65e-01	1.90
1/20	8.70e-03	1.94	4.30e-02	1.94
1/40	2.24e-03	1.96	1.14e-02	1.92
1/80	5.67e-04	1.98	2.93e-03	1.96
1/160	1.43e-04	1.99	7.42e-04	1.98

Example 2 (Homogeneous Media). In the second example, we consider the case of a homogeneous media when the values of the density and bulk modulus of compressibility are constants, that is, in (1.2)-(1.3) we set

$$\rho_1(x)=\rho_2(x)=K_1(x)=K_2(x)\equiv 2. \tag{4.1}$$

We take the initial data $\boldsymbol{U}(x,0)\equiv\mathbf{0}$ and the following boundary conditions:

$$u(0,t)=\begin{cases}-0.2\big(1+\cos\big(\pi(t-30)/30\big)\big), & \text{if}\quad t\le 60,\\ 0, & \text{if}\quad t>60,\end{cases}\qquad \sigma_x(0,t)\equiv 0$$

at the left boundary, and the free boundary condition at the right boundary. The Dirichlet boundary condition for u is implemented the same way as the Dirichlet boundary conditions were implemented in Example 1 and the free boundary conditions on the right and the boundary condition $\sigma_x(0,t)\equiv 0$ are implemented using the standard ghost cell technique. We apply the CU scheme with the MinMod2 reconstruction to the nonlinear elasticity system (1.1)-(1.3), (4.1) with $\beta=0.3$. The obtained results are shown in Fig. 3. As one can see, a shock wave clearly forms and it is nicely resolved by the CU scheme.

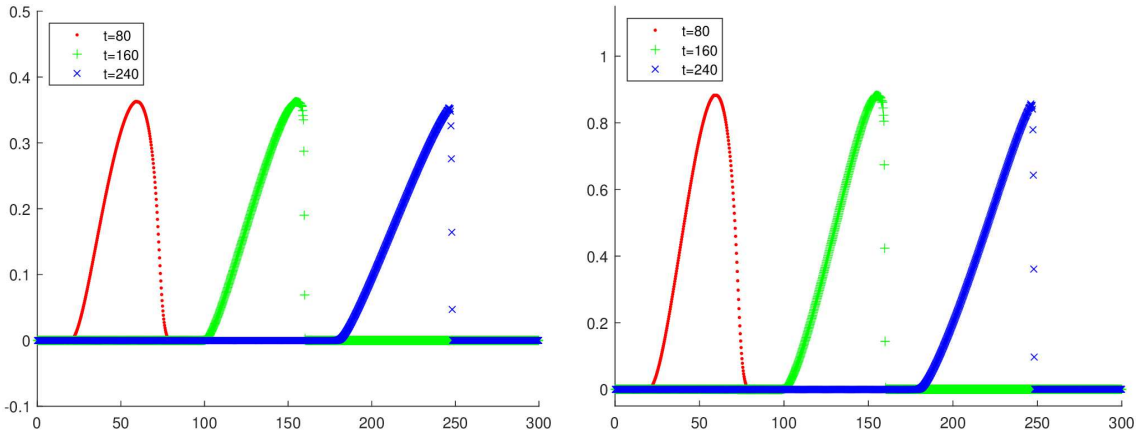

Figure 3: Example 2: Strain (left) and stress (right) computed by the CU scheme on a uniform mesh with $\Delta x=0.25$ at times $t=80,160,$ and 240.

Example 3 (Heterogeneous Media). In the third example, we consider the heterogeneous case with the density and bulk modulus of compressibility given by (1.2) with

$$\rho_1=K_1=3,\quad \rho_2=K_2=1,\quad \ell=1.$$

Compared to the homogeneous case, the situation changes dramatically. In Fig. 4, we show the strain and stress computed using 4 grid cells per layer of material at $t=80$. We compare the obtained results with the reference solution, computed by the LDCU scheme on a much finer grid with Δx=0.01 (our reference solution is in very good agreement with the solution presented in [18]). As one can see, the strain is reasonably resolved while the stress is very oscillatory.

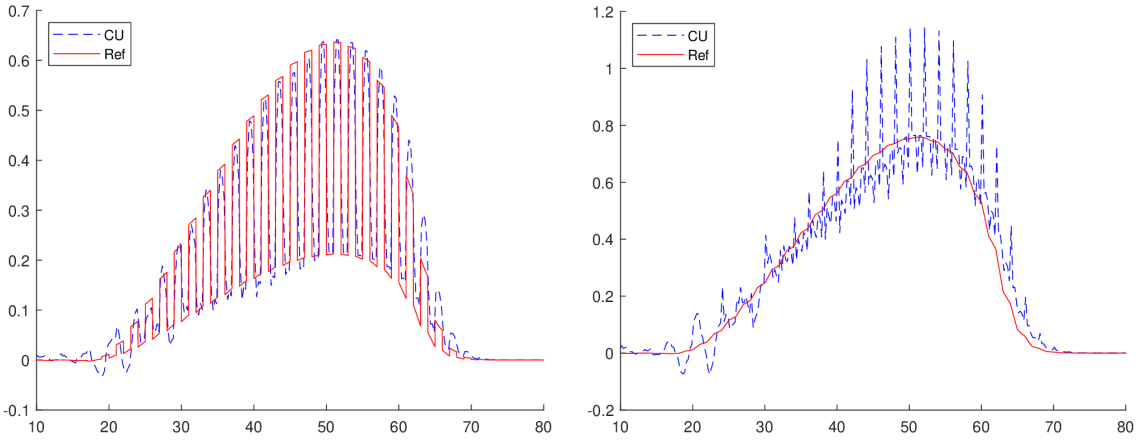

Figure 4: Example 3: Strain (left) and stress (right) computed by the CU scheme on a uniform mesh with $\Delta x=0.25$ (4 grid cells per layer of material) at time $t=80$.

We then increase the number of grid cells per layer to 16 and plot the obtained results in Fig. 5. As one can see, the strain is now nicely captured but the resolution of the stress has not improved. At a later time $t=240$, both components of the solution computed with 16 grid cells per layer is of poor quality. There is a noticeable phase shift in the strain (see Fig. 6, left) and the stress is not well resolved at all (see Fig. 6, right). The results reported in Figs. 5-6 clearly indicate that the CU scheme does not work properly.

Next, we apply the LDCU scheme to this example. We take the minmod parameter $\theta=2$ for small time calculations $(t\le 240)$ and $\theta=1.6$ for large times $(t\ge 840)$. In Fig. 7, we plot the strain and stress at times $t=80,160$, and 240 computed on a uniform mesh with $\Delta x=0.25$, or 4 grid cells per layer of material. One can clearly observe the formation and initial stages of the evolution of the waves with dispersive behavior. These results are in good agreement with the results reported in [18]. In Fig. 8, we show the solution at time $t=240$ from Fig. 7, but zoomed in closer. We compare it with the reference solution,

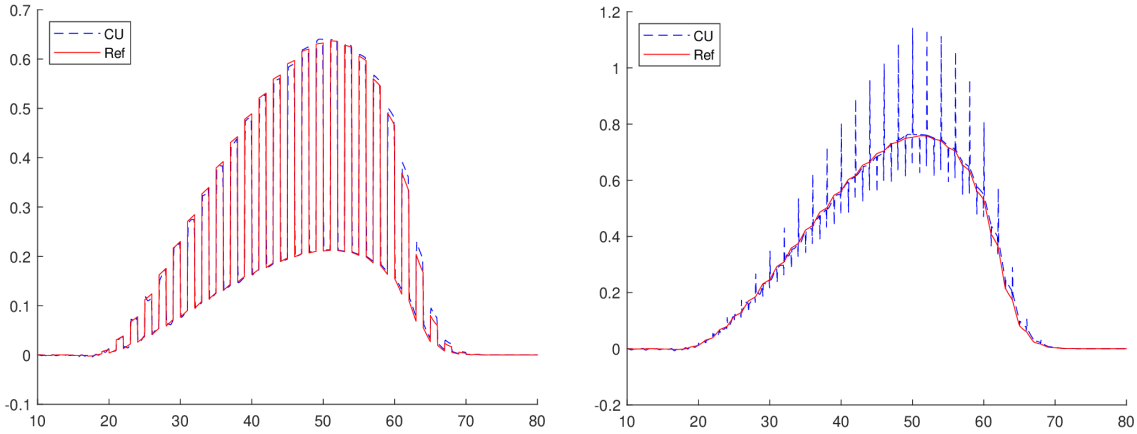

Figure 5: Example 3: Same as in Fig. 4, but with $\Delta x=0.0625$ (16 grid cells per layer of material).

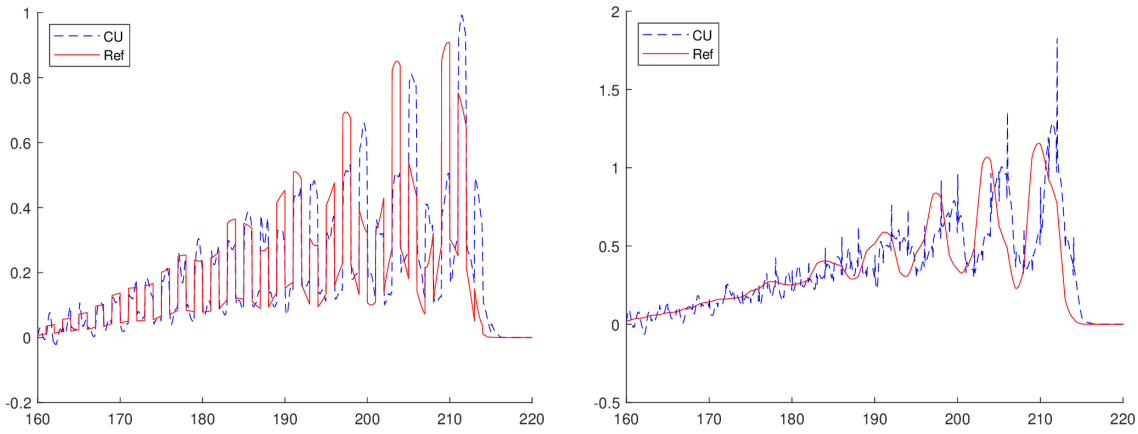

Figure 6: Example 3: Same as in Fig. 5, but at a later time $t=240$.

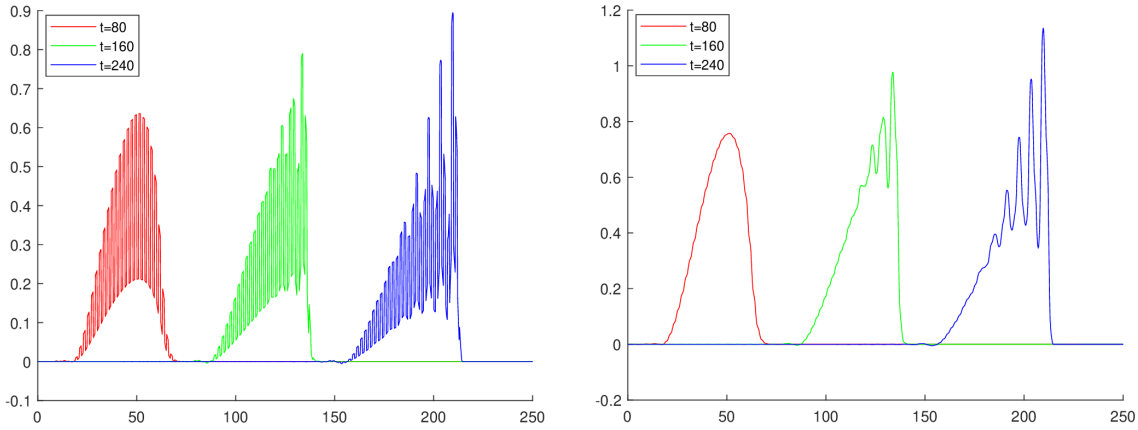

Figure 7: Example 3: Strain (left) and stress (right) computed by the LDCU scheme on a uniform mesh with $\Delta x=0.25$ (4 grid cells per layer of material) at times $t=80,160$, and 240.

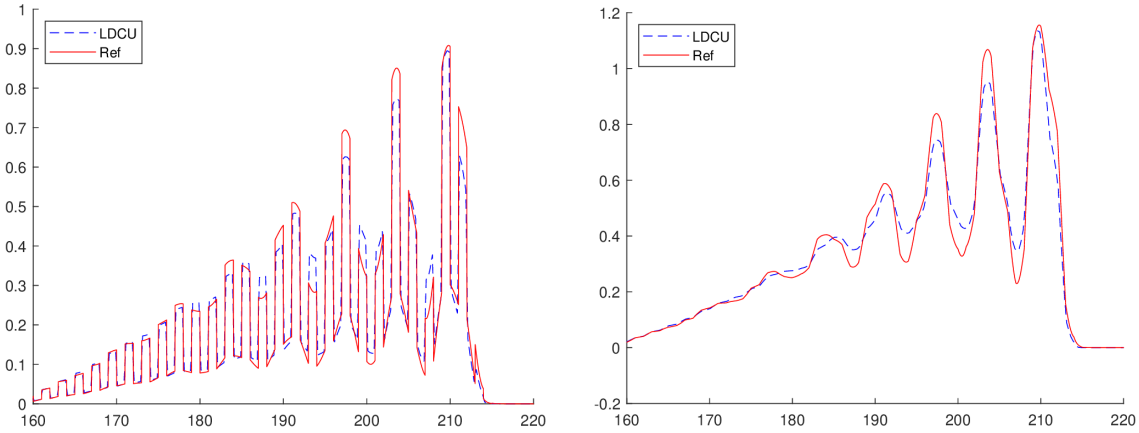

Figure 8: Example 3: Strain (left) and stress (right) computed by the LDCU scheme on a uniform mesh with $\Delta x=0.25$ (4 grid cells per layer of material) at time $t=240$.

computed by the LDCU scheme on a uniform mesh with $\Delta x=0.01$, which is 64 grid cells per layer of material. We can see that at 4 cells per layer, we already achieve fairly good resolution (compare this with the results reported in Fig. 6). We then double the number of cells per layer and present the obtained results in Fig. 9. Both the strain and stress are now nicely captured and the resolution of contact waves across material interfaces is almost perfect.

We now run the code for large times (up to $t=2850$). For $t>70$, we switch to the periodic boundary conditions, which are implemented using the standard ghost cell technique. The oscillations in the shock wave shown in Fig. 7 cause the heights of the waves to fluctuate which will result in the original wave to break up into solitary waves and propagate at different speeds. The results obtained by the LDCU scheme on a uniform mesh with $\Delta x=0.03125$ are shown in Fig. 10. At time $t=840$ our results are in good

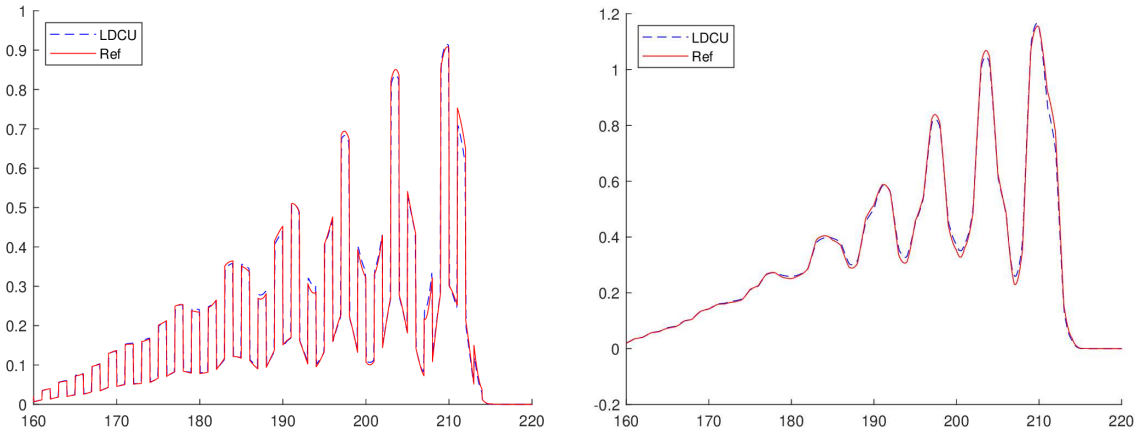

Figure 9: Example 3: Same as in Figure 8 but with $\Delta x = 0.125$ (8 grid cells per layer of material).

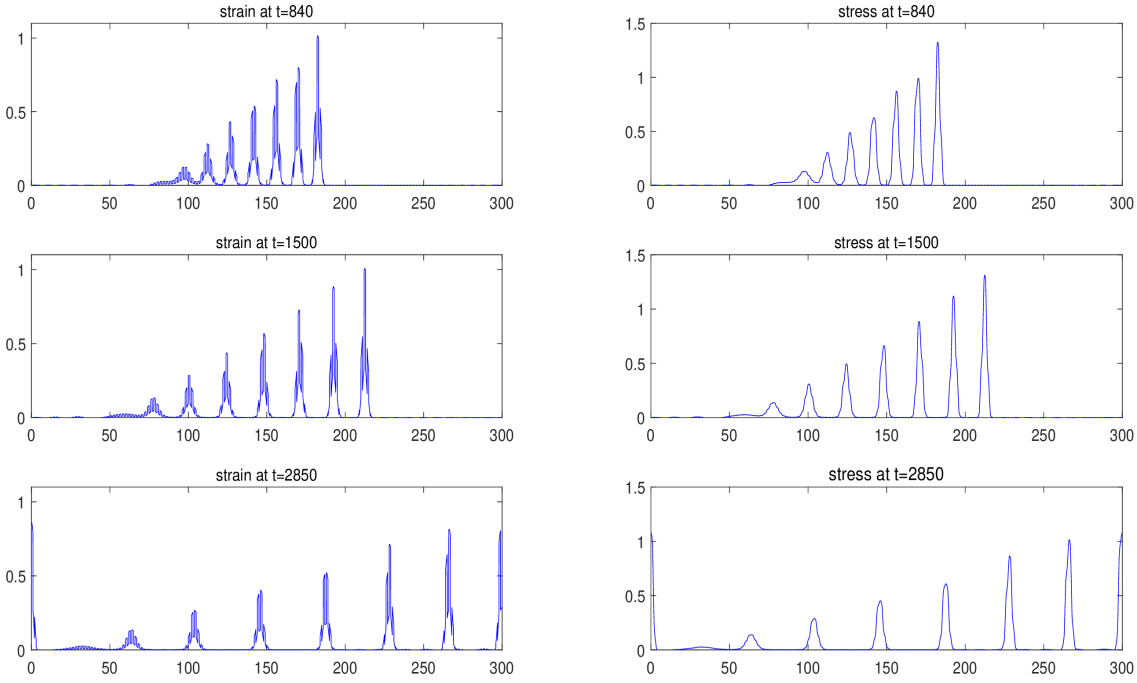

Figure 10: Example 3: Strain (left) and stress (right) computed by the LDCU scheme on a uniform mesh with $\Delta x = 0.03125$ at times $t = 840, 1500$, and 2850.

agreement with the ones computed by the wave propagation method from [18] on the same mesh; see the results reported in Fig. 11. For larger times ($t = 1500$ and 2850), the heights of the solitary waves computed by the LDCU schemes are substantially larger and thus they travel faster. We also compute the results of the wave propagation method on a much finer uniform mesh with $\Delta x = 0.01$, which are shown in Fig. 12. The solitary

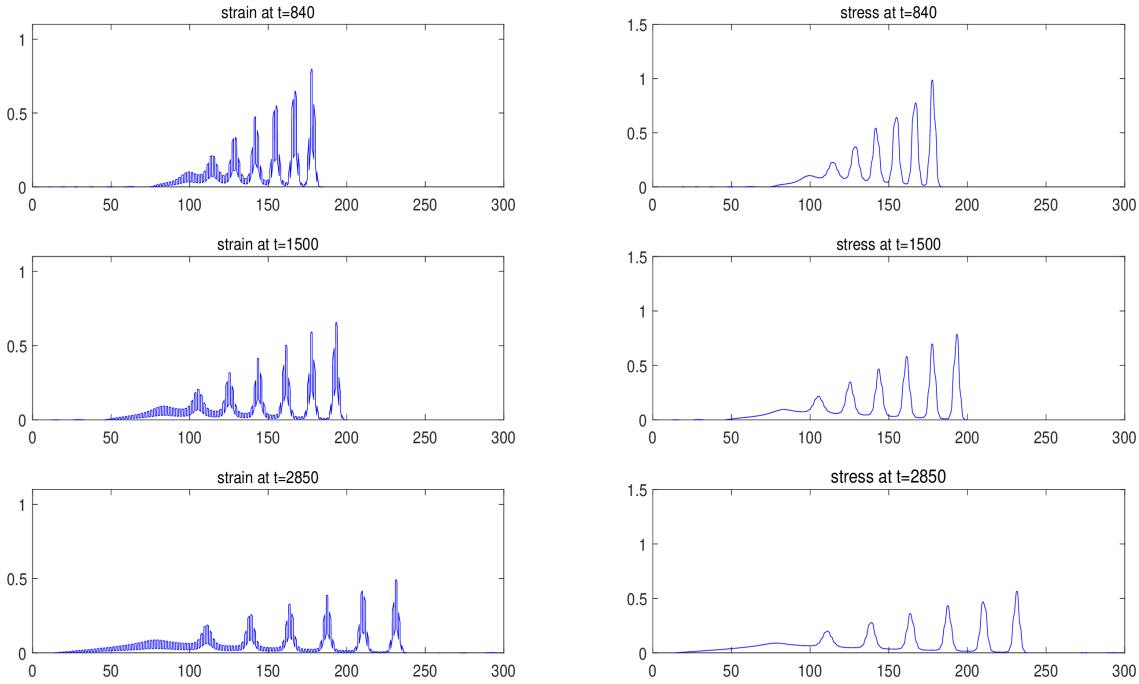

Figure 11: Example 3: Same as in Fig. 10, but computed using the wave propagation method.

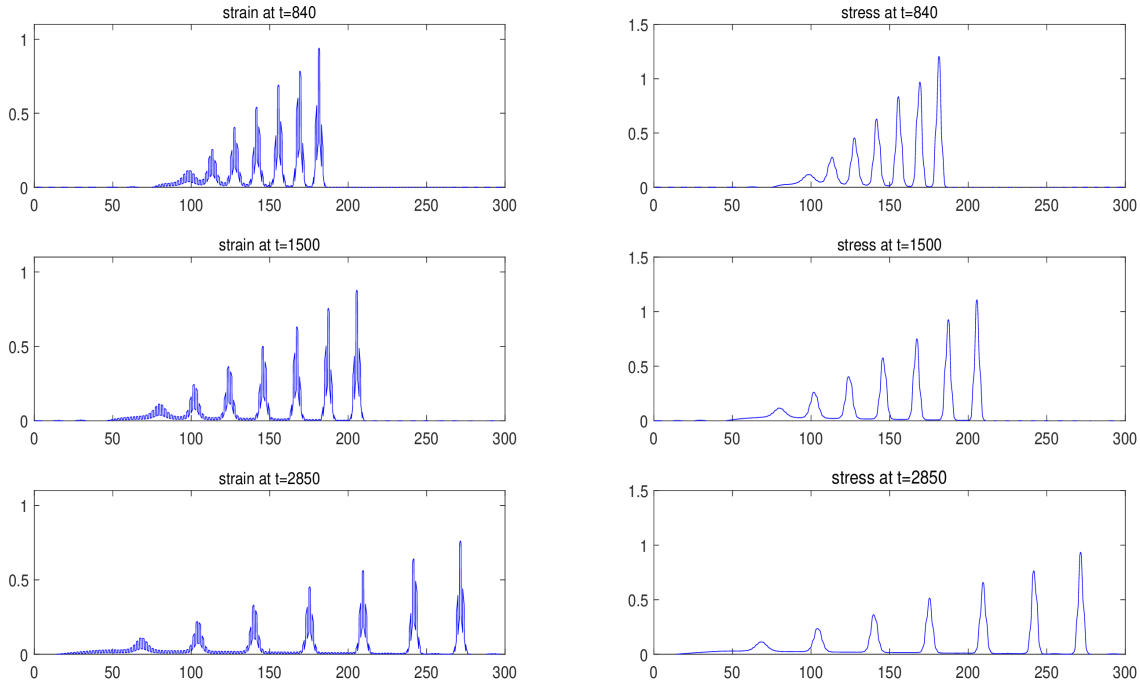

Figure 12: Example 3: Same as in Fig. 11, but computed on a finer mesh with $\Delta x = 0.01$.

waves travel faster compared to those computed on a coarser mesh (Fig. 11), but they still travel slower than the waves captured by the LDCU scheme. This occurs thanks to a smaller amount of numerical dissipation present in the LDCU scheme so that the solitary waves are (almost) not damped by the LDCU scheme.

4.2 Two-dimensional example

Example 4 (2-D Heterogeneous Media). In the 2-D example, we take the problem setting from [12]: We use the stress-strain relation (1.4) and consider the domain $[0,100]\times[0,10]$ with alternating vertical material strips of length 1 (as outlined in Fig. 13) so that, for all integer $j\geq 0$,

$$\rho(x,y)=\begin{cases}4, & \text{if} \quad 2j<x<2j+1,\\ 1, & \text{otherwise,}\end{cases} \qquad K(x,y)=\begin{cases}4, & \text{if} \quad 2j<x<2j+1,\\ 1, & \text{otherwise.}\end{cases}$$

The initial condition is a half of a Gaussian,

$$\sigma(x,y,0)=5e^{-\frac{x^2+(y-5)^2}{25}}, \quad x>0$$

with $u(x,y,0)=v(x,y,0)\equiv 0$. The boundary conditions are periodic in the y-direction and reflexive in the x-direction. They are implemented using the standard ghost cell technique.

As one can see in Figs. 14 and 15, by time $t=75$, the waves have started to evolve into solitary waves. One can also see that while the strain develops contact discontinuities (see Fig. 14), the stress remains continuous (see Fig. 15). Figs. 16 and 17 show 1-D slices along the line $y=5$ of the strain and stress, respectively. As one can see, the strain and stress behave in a similar fashion to the 1-D case. The oscillations in the shock wave for the strain will cause the heights of the wave to fluctuate which results in the different parts of the wave traveling at different speeds. The resolution achieved by the LDCU scheme is quite spectacular given that only 4 cells in the x-direction per a vertical layer of material have been used (in the presented calculations $\Delta x=\Delta y=0.25$). As in the 1-D case, no oscillations across material interfaces have been observed.

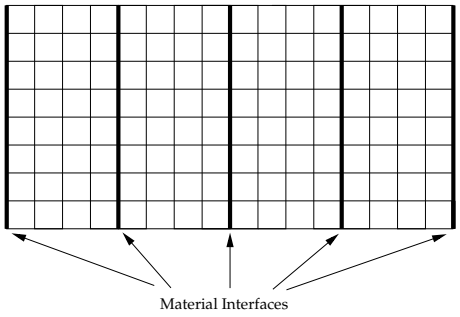

Figure 13: Example 4: Layout of materials and a sample of adjusted 2-D Cartesian grid.

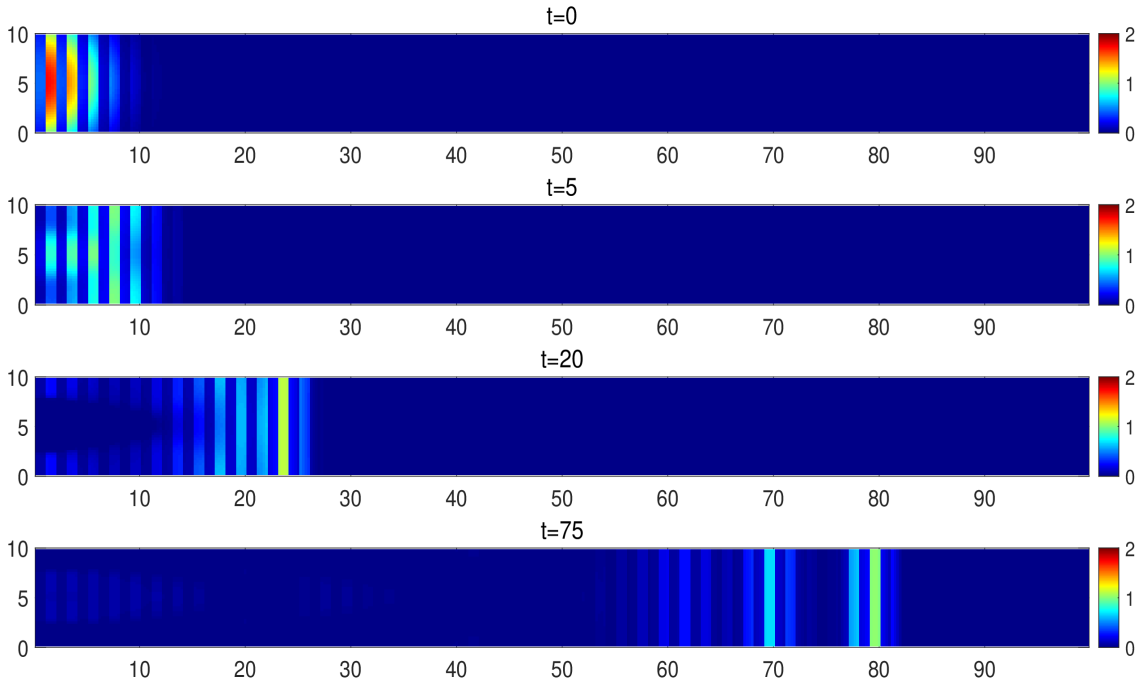

Figure 14: Example 4: Strain at times $t=0,5,20$, and 75.

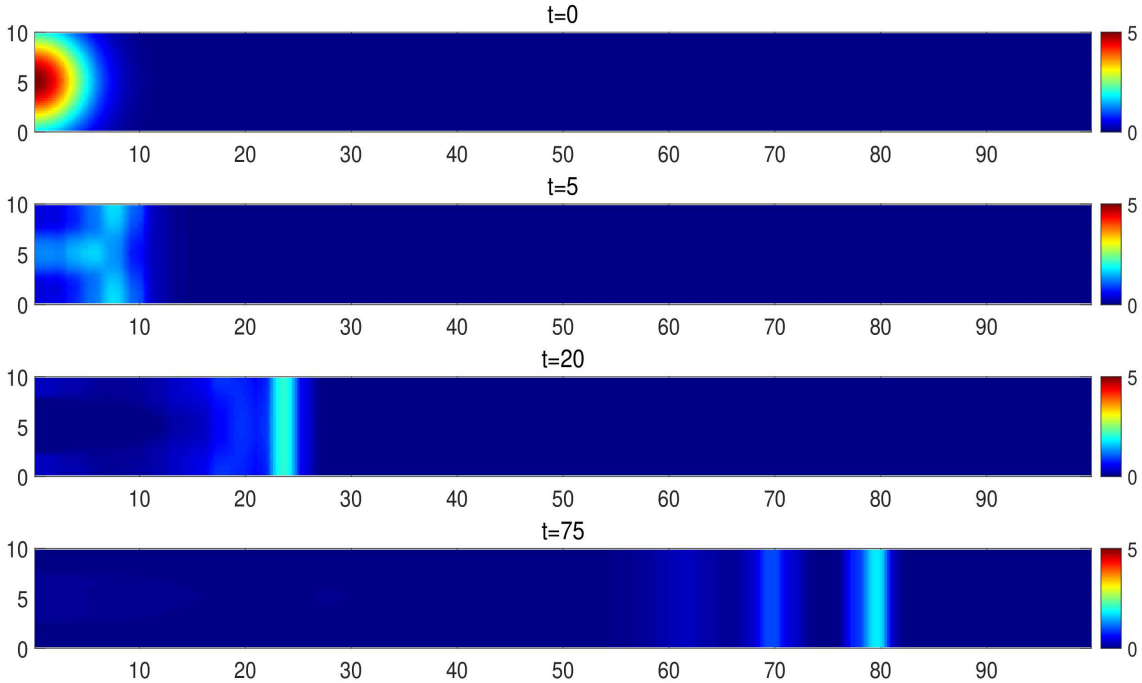

Figure 15: Example 4: Stress at times $t=0,5,20$, and 75.

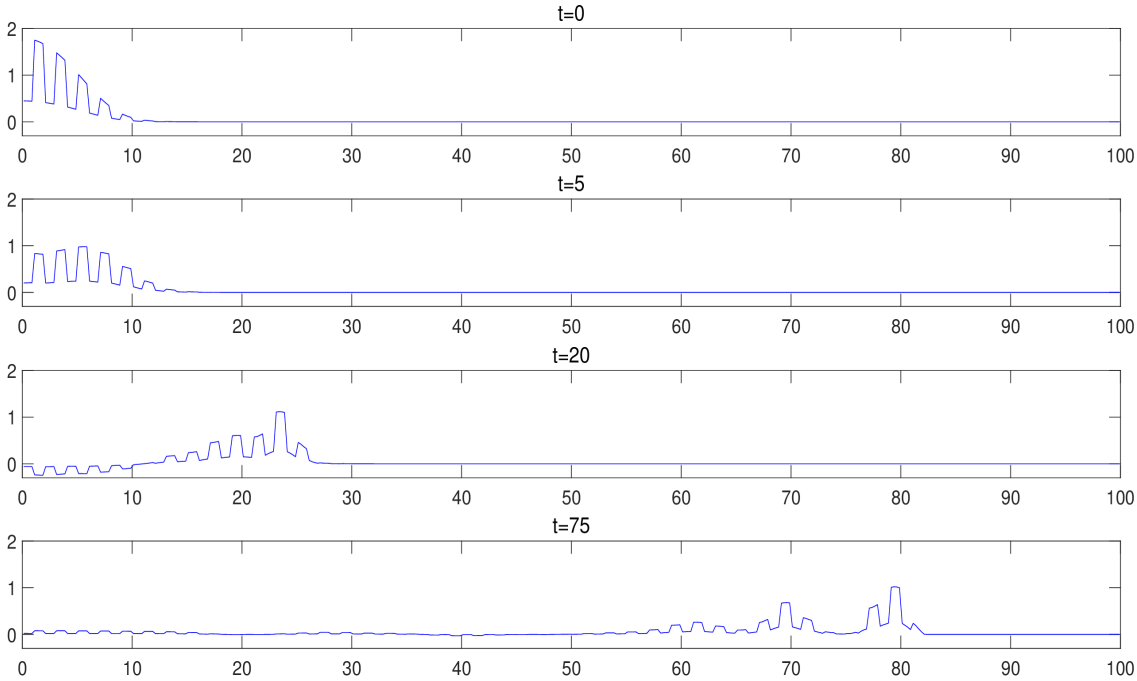

Figure 16: Example 4: 1-D slices of strain at times $t=0,5,20$, and 75.

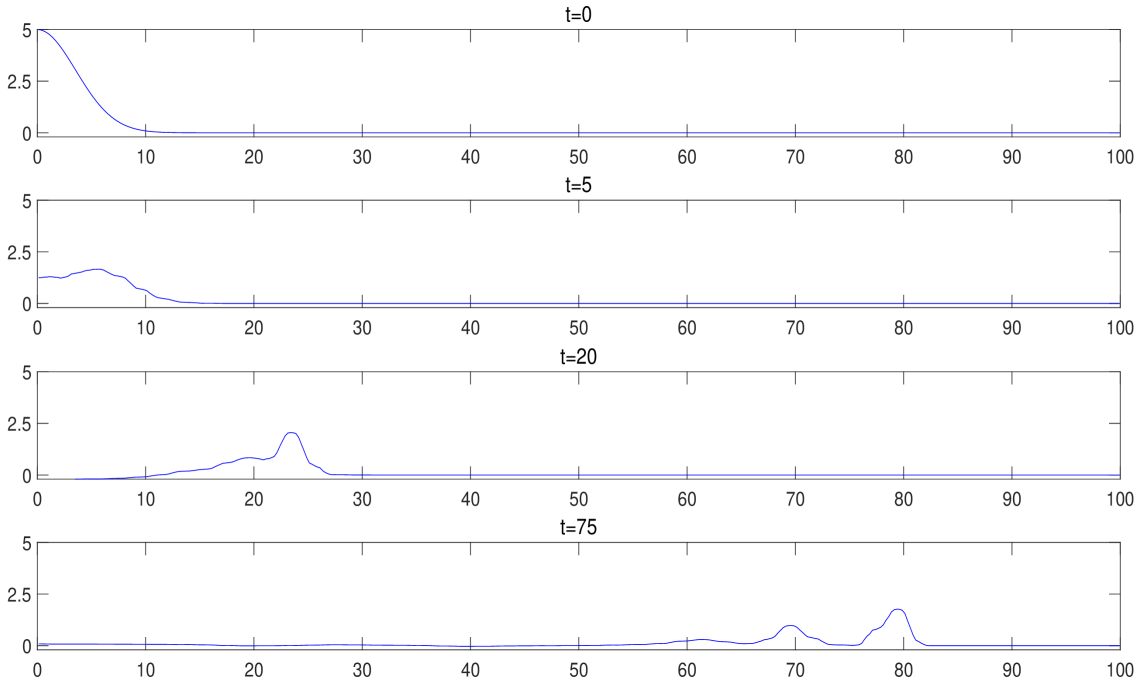

Figure 17: Example 4: 1-D slices of stress at times $t=0,5,20$, and 75.

Acknowledgments

The work of A. Kurganov was supported in part by the NSFC (Grant No. 12171226) and by the Fund of the Guangdong Provincial Key Laboratory of Computational Science and Material Design (Grant No. 2019B030301001).

References

[1] M. Ben-Artzi and J. Falcovitz, *Generalized Riemann Problems in Computational Fluid Dynamics*, in: *Cambridge Monographs on Applied and Computational Mathematics*, Vol. 11, Cambridge University Press, 2003.
[2] S. Chabot, N. Glinsky, E. D. Mercerat, and L. F. Bonilla Hidalgo, A high-order discontinuous Galerkin method for 1D wave propagation in a nonlinear heterogeneous medium, *J. Comput. Phys.*, 355:191–213, 2018.
[3] A. Chertock, S. Chu, M. Herty, A. Kurganov, and M. Lukáčová-Medviďová, Local characteristic decomposition based central-upwind scheme, *J. Comput. Phys.*, 473:111718, 2023.
[4] S. Chu, A. Kurganov, and R. Xin, A fifth-order A-WENO scheme based on the low-dissipation central-upwind fluxes, in: *Hyperbolic Problems: Theory, Numerics, Applications. Vol. II. HYP 2022, SEMA SIMAI Springer Series*, Vol. 35, Springer, 51–61, 2024.
[5] S. Chu, A. Kurganov, and R. Xin, Low-dissipation central-upwind schemes for compressible multifluids, *J. Comput. Phys.*, 518:113311, 2024.
[6] T. Fogarty and R. J. LeVeque, High-resolution finite volume methods for acoustics in periodic or random media, *J. Acoust. Soc. Am.*, 106:17–28, 1999.
[7] E. Godlewski and P.-A. Raviart, *Numerical Approximation of Hyperbolic Systems of Conservation Laws*, in: *Applied Mathematical Sciences*, Vol. 118, Springer-Verlag, 2021.
[8] S. Gottlieb, D. Ketcheson, and C.-W. Shu, *Strong Stability Preserving Runge-Kutta and Multistep Time Discretizations*, World Scientific Publishing Co., Inc., 2011.
[9] S. Gottlieb, C. Shu, and E. Tadmor, Strong stability-preserving high order time discretization methods, *SIAM Rev.*, 43:89–112, 2001.
[10] J. S. Hesthaven, *Numerical Methods for Conservation Laws: From Analysis to Algorithms*, in: *Computational Science and Engineering*, SIAM, 2018.
[11] G.-S. Jiang and E. Tadmor, Nonoscillatory central schemes for multidimensional hyperbolic conservation laws, *SIAM J. Sci. Comput.*, 19:1892–1917, 1998.
[12] D. Ketcheson, *High Order Strong Stability Preserving Time Integrators and Numerical Wave Propagation Methods for Hyperbolic PDEs*, PhD Thesis, University of Washington, 2009.
[13] A. Kurganov and C.-T. Lin, On the reduction of numerical dissipation in central-upwind schemes, *Commun. Comput. Phys.*, 2:141–163, 2007.
[14] A. Kurganov, S. Noelle, and G. Petrova, Semi-discrete central-upwind scheme for hyperbolic conservation laws and Hamilton-Jacobi equations, *SIAM J. Sci. Comput.*, 23:707–740, 2001.
[15] A. Kurganov and E. Tadmor, New high resolution central schemes for nonlinear conservation laws and convection-diffusion equations, *J. Comput. Phys.*, 160:241–282, 2000.
[16] A. Kurganov and R. Xin, New low-dissipation central-upwind schemes, *J. Sci. Comput.*, 96:56, 2023.
[17] R. LeVeque, *Finite Volume Methods for Hyperbolic Problems*, in: *Cambridge Texts in Applied Mathematics*, Cambridge University Press, 2002.

[18] R. LeVeque, Finite volume methods for non-linear elasticity in heterogeneous media, *Internat. J. Numer. Methods Fluids*, 40:93–104, 2002.
[19] R. LeVeque and D. Yong, Phase plane behavior of solitary waves in nonlinear layered media, in: *Hyperbolic Problems: Theory, Numerics, Applications*, Springer, 43–51, 2003.
[20] R. LeVeque and D. Yong, Solitary waves in layered nonlinear media, *SIAM J. Appl. Math.*, 63:1539–1560, 2003.
[21] K.-A. Lie and S. Noelle, An improved quadrature rule for the flux-computation in staggered central difference schemes in multidimensions, *J. Sci. Comput.*, 63:1539–1560, 2003.
[22] K.-A. Lie and S. Noelle, On the artificial compression method for second-order nonoscillatory central difference schemes for systems of conservation laws, *SIAM J. Sci. Comput.*, 24:1157–1174, 2003.
[23] H. Nessyahu and E. Tadmor, Nonoscillatory central differencing for hyperbolic conservation laws, *J. Comput. Phys.*, 87:408–463, 1990.
[24] D.-L. Qiao, P. Zhang, Z.-Y. Lin, S. Wong, and K. Choi, A Runge-Kutta discontinuous Galerkin scheme for hyperbolic conservation laws with discontinuous fluxes, *Appl. Math. Comput.*, 292:309–319, 2017.
[25] P. Sweby, High resolution schemes using flux limiters for hyperbolic conservation laws, *SIAM J. Numer. Anal.*, 21:995–1011, 1984.
[26] E. Toro, *Riemann Solvers and Numerical Methods for Fluid Dynamics: A Practical Introduction*, Springer-Verlag, 2009.
[27] B. van Leer, Towards the ultimate conservative difference scheme. V. A second-order sequel to Godunov's method, *J. Comput. Phys.*, 32:101–136, 1979.
[28] Z. Xu, P. Zhang, and R. Liu, δ-mapping algorithm coupled with WENO reconstruction for nonlinear elasticity in heterogeneous media, *Appl. Numer. Math.*, 57:103–116, 2007.
[29] P. Zhang and R. Li, Hyperbolic conservation laws with space-dependent flux: I. Characteristics theory and Riemann problem, *J. Comput. Appl. Math.*, 156:1–21, 2003.
[30] P. Zhang and R. Li, Hyperbolic conservation laws with space-dependent flux: II. General study of numerical fluxes, *J. Comput. Appl. Math.*, 176:105–129, 2005.